

HARD X-RAY EMISSION FROM THE M87 AGN DETECTED WITH *NUSTAR*KA-WAH WONG^{1,2}, RODRIGO S. NEMMEN³, JIMMY A. IRWIN⁴, AND DACHENG LIN⁵,
Astrophysical Journal Letters

ABSTRACT

M87 hosts a 3–6 billion solar mass black hole with a remarkable relativistic jet that has been regularly monitored in radio to TeV bands. However, hard X-ray emission $\gtrsim 10$ keV, which would be expected to primarily come from the jet or the accretion flow, had never been detected from its unresolved X-ray core. We report *NuSTAR* detection up to 40 keV from the the central regions of M87. Together with simultaneous *Chandra* observations, we have constrained the dominant hard X-ray emission to be from its unresolved X-ray core, presumably in its quiescent state. The core spectrum is well fitted by a power law with photon index $\Gamma = 2.11^{+0.15}_{-0.11}$. The measured flux density at 40 keV is consistent with a jet origin, although emission from the advection-dominated accretion flow cannot be completely ruled out. The detected hard X-ray emission is significantly lower than that predicted by synchrotron self-Compton models introduced to explain emission above a GeV.

Subject headings: accretion, accretion disks — black hole physics — galaxies: elliptical and lenticular, cD — galaxies: individual (M87) — galaxies: nuclei — X-rays: galaxies

1. INTRODUCTION

One of the best-studied active galactic nuclei (AGNs) is located at the center of the nearby radio galaxy M87. The giant elliptical galaxy hosts a ~ 3 –6 billion solar mass supermassive black hole (SMBH; Macchetto et al. 1997; Gebhardt & Thomas 2009), and contains the first extragalactic astrophysical jet discovered (Curtis 1918). Its proximity ($D=16$ Mpc, $1''=78$ pc; Tonry et al. 2001) allows us to resolve the arcsecond-scale relativistic jet near the nucleus region with radio (~ 40 micro-arcsecond: 230 GHz high frequency VLBI; Doleman et al. 2012), optical (0.1 arcsec: *HST*), and X-ray (sub-arcsecond: *Chandra*) observations. It is also a very-high-energy (VHE; >100 GeV) source detected with the *Fermi*, H.E.S.S., VERITAS, and MAGIC γ -ray telescopes (see, Abramowski et al. 2012, and references therein), and one of the few radio galaxies with TeV γ -rays detected but not strongly beamed.⁶ This provides a different scientific angle to study high-energy particle acceleration mechanisms in AGNs with misaligned jets.

Multi-wavelength observations resolve the M87 central region into different components at different angular scales: a core where the SMBH is located, a jet, and multiple knots along the jet direction (e.g., Biretta et al. 1999; Junor et al. 1999; Kovalev et al. 2007; Harris et al. 2009). The most obvious features on *Chandra* X-ray images are the core and the bright knots (hereafter, core means the central source unresolved by *Chandra* at the sub-arcsecond scale, following the definition in Figure 1

of Harris et al. (2006); see also the right panel of Figure 1 below). Outbursts at different wavelengths have been seen from both the core and knots (Harris et al. 2009; Abramowski et al. 2012). The locations of the highest energy burst (GeV–TeV) are not very clear. For example, it had been suggested that the HST-1 knot outburst is responsible for the TeV outburst seen in 2005 (Aharonian et al. 2006). However, later observations, particularly with *Chandra*, support that the TeV emission comes from the unresolved *Chandra* core (Abramowski et al. 2012). The exact origin of the different energy emission is still under debate. Studying the full spectral energy distribution (SED) at different states (quiescence or flare) of the core and knots will hopefully help us to distinguish different models (e.g., Nemmen et al. 2014; de Jong et al. 2015; Prieto et al. 2016).

X-rays penetrate the dust-free M87 nucleus (e.g., Perlman et al. 2001) directly from the inner most accretion regions of the flow, allowing us to study physics down to the event horizon scale. Because it is a low-luminosity AGN (LLAGN) with an Eddington ratio of 3.6×10^{-6} (Prieto et al. 2016), the SMBH is believed to be accreting as an advection-dominated accretion flow (ADAF; see, e.g., Yuan & Narayan 2014, for a review). The X-ray emission from the M87 core is believed to come from either the ADAF or the (unresolved) jet, therefore studying the X-ray emission will provide constraints on these models (Nemmen et al. 2014). Although X-ray emission $\lesssim 10$ keV has been studied in detail, hard X-rays above that threshold had never been detected from the core.⁷ In this Letter, we report the detection of hard X-ray emission from the core up to 40 keV, with simultaneous *NuSTAR* and *Chandra* observations. Errors are given at the 90% confidence level unless otherwise specified.

2. X-RAY OBSERVATIONS

⁷ de Jong et al. (2015) detected hard X-ray emission observed with *Suzaku* in 2006, which likely comes from HST-1.

kw6k@email.virginia.edu

¹ Eureka Scientific, Inc., 2452 Delmer Street Suite 100, Oakland, CA 94602-3017, USA

² Department of Physics and Astronomy, Minnesota State University, Mankato, MN 56001, USA

³ Universidade de São Paulo, Instituto de Astronomia, Geofísica e Ciências Atmosféricas, São Paulo, SP 05508-090, Brazil

⁴ Department of Physics and Astronomy, University of Alabama, Box 870324, Tuscaloosa, AL 35487, USA

⁵ Space Science Center, University of New Hampshire, Durham, NH 03824, USA

⁶ The others are Cen A, NGC 1275, and IC 310.

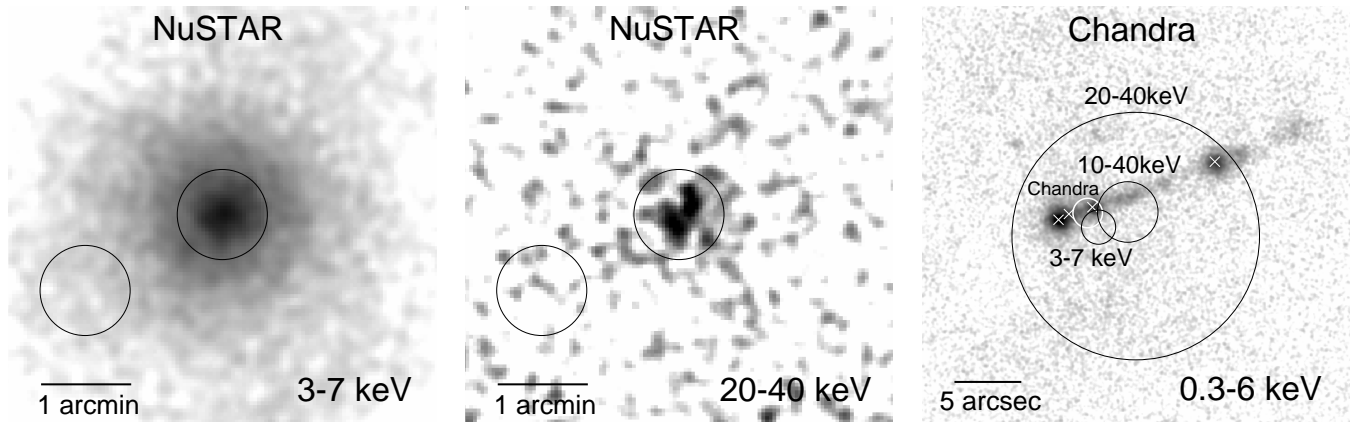


FIG. 1.— Smoothed 3–7 keV (left) and 20–40 keV (middle) *NuSTAR* images of M87. The circle at the center of the image indicates the 30'' radius spectral extraction region. The circle in the lower left is the background spectral extraction region with the same radius of 30''. A smoothed 0.3–6 keV *Chandra* image is shown in the right panel. The four white crosses from the left to the right are the locations of the core, the HST-1 knot, knot D, and knot A, respectively. The three black solid circles indicate the 3σ position errors of the emission peaks measured with *NuSTAR* in different energy bands. The white circle indicates the *Chandra* position determined using a smoothed image in the 3–7 keV band (see the text).

M87 was observed with *NuSTAR* on 2017 February 15, April 11, and April 14 for 50, 24, and 22 ks, respectively (ObsIDs: 60201016002, 90202052002, and 90202052004). All data were reduced using the *HEASoft* v6.21 and *CALDB* version 20170616. We have reprocessed the data using the *nupipeline* script of the *NuSTAR* Data Analysis Software (*NuSTARDAS*) package with the standard screening criteria. Four *Chandra* snapshots were taken during the three *NuSTAR* observations on 2017 February 15, February 16, April 11, April 14 for 5, 5, 13, and 13 ks, respectively (ObsIDs: 19457, 19458, 20034, and 20035). All the data were reprocessed using the *Chandra* Interactive Analysis of Observations (*CIAO*) software version 4.9 and the *Chandra* *CALDB* version 4.7.4.

Figure 1 shows the *NuSTAR* images in 3–7 keV and 20–40 keV. Each image was created by combining the three observations and the two detectors. Relative astrometry was corrected by matching the centroids of the 3–7 keV emission. Hard X-ray emission in 20–40 keV is clearly detected at 7σ .

To quantify the spatial structure of the hard X-ray (20–40 keV) emission, we fit the hard X-ray image with two 2D Gaussian models to represent the PSF core and larger PSF wing and a constant background model. The fitting region is limited to a circular region of radius $\sim 2'$ centered near the peak of the emission. The fitted FWHM is consistent with the 18'' FWHM of the *NuSTAR* PSF, indicating that the hard X-ray emission is unresolved. The location of the hard X-ray peak can be determined to about 9'' at 3σ for two parameters of interest, and the confidence region is shown in the right panel of Figure 1. Using a wider hard band in 10–40 keV, the error circle has a smaller radius of $2''.3$. In contrast, the soft X-ray emission in 3–7 keV is clearly extended due to the strong intracluster medium (ICM) emission. We determined the location of the soft X-ray peak by fitting a 2D Gaussian plus a 2D β -model with a constant background. We tied the centers of the first two azimuthally symmetric models and thawed all the remaining parameters. The much smaller ($\sim 1''$) confidence region is also shown in the figure.

The peak location of the 10–40 keV hard X-ray emis-

sion is marginally consistent with the softer 3–7 keV peak. Thus, the origin of the hard X-ray emission above 10 keV is consistent with the origin of the softer emission (i.e., core/knots/jet emission contaminated by ICM). Deeper *NuSTAR* observations can potentially distinguish any structure to better than a few arcsec.

The location of the *NuSTAR* soft peak can be compared with that measured with *Chandra*. We have smoothed a *Chandra* 3–7 keV image with a 2D Gaussian to simulate the FWHM of the *NuSTAR* PSF (18''). The confidence region of the smoothed *Chandra* image is located near knot D. It is only slightly offset by about 1'' from the *NuSTAR* soft peak, which is much smaller than the 8'' absolute astrometric uncertainty for *NuSTAR*.

We extracted *NuSTAR* spectra from the nuclear region of M87 for all the three observations and created the corresponding response files for the point source. The extraction region is circular with a 30'' radius, which is close to the 29'' half-power radius, centered at the *NuSTAR* 3–7 keV peak (Figure 1). The background circular region with the same radius was chosen to be far enough from the center and also located on the same detector chip as the source. The latter criterion is important to minimize instrumental background variations from chip to chip (Wik et al. 2014a). Since the individual spectra are consistent with each other, we combined all the *NuSTAR* spectral and response files using the *FTOOL* *addspec*.

The unresolved *NuSTAR* X-ray emission is mainly contributed by the X-ray core, the jet and knots along the jet, the diffuse ICM, and unresolved low-mass X-ray binaries (LMXBs). With simultaneous observations and archival *Chandra* data, these individual components can be well constrained. We first detected point sources using the *Chandra* data following the procedure described in Wong et al. (2014). To detect fainter sources, we also included two deeper *Chandra* observations taken in 2016 (ObsIDs: 18838 and 18856 for 56 and 25 ks, respectively). We extracted *Chandra* spectra from the six observations with detected point sources inside the *NuSTAR* spectral extraction region that are unrelated to the core, jet, or knots. Each spectral region is circular with a radius of 1''. A corresponding local annular background with inner

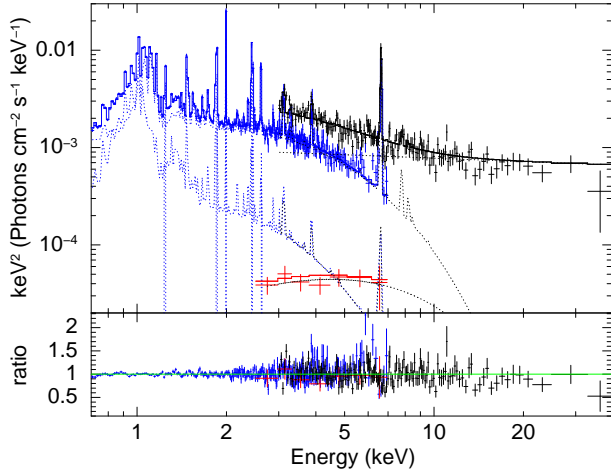


FIG. 2.— *NuSTAR* spectrum (black) within a circular region of $30''$ centered on the X-ray peak joint-fitted with the *Chandra* ICM (blue) and LMXB (red) spectra. The dashed lines are the individual components discussed in the text. The vertical dashed blue lines below 3 keV are the Gaussian models, to take into account the line emission. Beyond ~ 5 keV, the X-ray emission is dominated by the AGN-related activities (core, knots, and jet) and is completely dominated by these activities beyond ~ 15 keV. Error bars are at 1σ .

and outer radii of $1''$ and $2''$, respectively, is centered on each source. The combined spectrum is used to constrain the LMXB component.

To constrain the jet component, we extracted *Chandra* spectra using a $19''.5 \times 3''$ rectangular region enclosing all the jet and knots (but not the unresolved *Chandra* core or HST-1). A local background with two similar rectangular regions adjacent to the source region is used.

For both the core and the HST-1 knot, we extracted *Chandra* spectra with circular regions of $0''.4$ radius centered on them and created the corresponding response files for the point sources. For the core, a pie-shaped local background with inner and outer radii of $2''$ and $4''$, respectively, centered on the core and away from HST-1 is used. For HST-1, a circular region of $0''.4$ radius opposite from the core is chosen as its local background. For the core, jet, and HST-1 spectra, only the simultaneous observations taken in 2017 were used. The core and HST-1 were in their low states during the 2017 observations and their total pile-up fraction is not significant (3–7%).⁸

The remaining component is mostly the steady ICM emission. Since the *NuSTAR* background spectrum also contains ICM emission (and a negligible contribution from LMXBs), we extracted *Chandra* ICM spectra from the same *NuSTAR* source and background regions to take into account this component. The abovementioned *Chandra* observations were taken in the 1/8-subarray mode that do not cover the *NuSTAR* background region. Therefore, we selected earlier *Chandra* archival data (ObsIDs: 352, 2707, 3717, and 8517) that cover both the *NuSTAR* source and background regions. The total cleaned exposure time is ~ 110 ks, similar to that of the six *Chandra* observations used to extract the LMXB spectra. We removed all the point sources detected with the same method used for the *Chandra* ICM source and

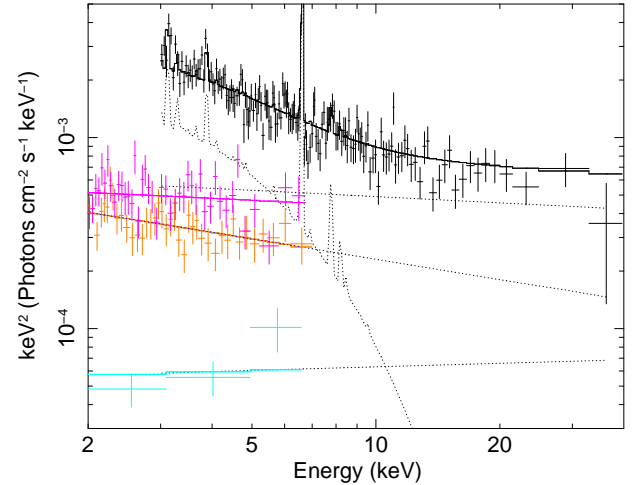


FIG. 3.— Same as Figure 2 but the extra core (magenta; upper), jet (orange; middle), and HST-1 (cyan; lower) components are also joint-fitted. The three power-law dashed lines are models for these extra components best-fitted to the *NuSTAR* data. The curved dashed line is the hotter ICM component. For clarity, the cooler ICM and LMXB components and the residual panel are not shown.

background spectra.

3. OVERALL HARD X-RAY EMISSION FROM AGN ACTIVITIES

To constrain the overall hard X-ray emission from the AGN activities, which includes the unresolved X-ray core, knots, and the jet, we fitted the *NuSTAR* spectrum jointly with the *Chandra* ICM and LMXB spectra. All the spectra were grouped with a minimum of one count per bin and were fitted using the *C*-statistic in the X-ray Spectral Fitting Package (XSPEC).⁹ Errors of spectral parameters were determined by assuming $\Delta C = 2.706$ (90% confidence) for one parameter of interest. The *Chandra* ICM spectrum in the 0.7–7.0 keV range was well fitted with an absorbed two-temperature thermal model (PHABS*(APEC+APEC); see also Russell et al. 2015). We fixed the absorption at the Galactic value of $N_H = 1.94 \times 10^{20} \text{ cm}^{-2}$ (Kalberla et al. 2005), metallicity at solar value (Russell et al. 2015), and redshift at $z = 0.004283$ (Cappellari et al. 2011). The two temperatures and the two normalizations were free parameters. We have also taken into account some residual ICM line emissions below 3 keV by adding five GAUSSIAN models with zero line width, although ignoring these will not have any impact on our results.

The *Chandra* LMXB spectrum between ~ 2 and 7 keV was fitted using a template given by Revnivtsev et al. (2014), which is based on the broadband 3–100 keV spectrum of M31 dominated by LMXBs and is consistent with the Galactic bulge emission (Krivonos et al. 2007).¹⁰ We fixed the shape of the adopted spectrum but varied its overall normalization. Since the LMXB component in the *NuSTAR* spectrum is subdominant (see Figure 2 below), increasing the normalization by a factor of two or using different LMXB models (e.g., a single power-law model or even a broken power-law template used by Wik et al. (2014b) to actually fit the harder high-mass

⁸ The pile-up effect on spectral slope, determined by fitting a pileup model, is always \lesssim the statistical uncertainty.

⁹ <http://heasarc.nasa.gov/xanadu/xspec/>

¹⁰ Note that the first power-law index in the equation given by Revnivtsev et al. (2014) should be -0.5 .

TABLE 1
BEST-FIT SPECTRAL RESULTS

Name	Γ^a	K^b	$f_{20-40\text{ keV}}^c$
Core+HST-1+Jet	$2.12^{+0.12}_{-0.13}$	102^{+38}_{-29}	$7.7^{+1.1}_{-1.0}$
Core	$2.11^{+0.15}_{-0.11}$	63^{+28}_{-15}	$4.8^{+0.9}_{-1.0}$
HST-1	[1.94]	$5.5^{+1.0}_{-0.9}$	$0.7^{+0.1}_{-0.1}$
Jet	$2.36^{+0.16}_{-0.17}$	52^{+10}_{-10}	$1.8^{+0.9}_{-0.6}$

Notes. The C -statistic in fitting the overall emission is $C = 1473$ for 1269 degrees of freedom, while $C = 2091$ when decomposing the different components for 1960 degrees of freedom.

^a Power-law photon index. For HST-1, the parameter cannot be constrained during the joint fitting and is fixed to the value determined with *Chandra* alone.

^b Normalization in units of 10^{-5} photons $\text{keV}^{-1} \text{cm}^{-2} \text{s}^{-1}$ at 1 keV.

^c Flux in units of $10^{-13} \text{erg cm}^{-2} \text{s}^{-1}$.

binary dominated sources) gives essentially the same results.

The 3–40 keV *NuSTAR* spectrum was joint-fitted with the *Chandra* ICM and LMXB spectra by including these two component models as well as a single power-law model to represent the combined emission from the core, knots, and the jet. The same Galactic absorption model was also used for all the components. We tied all the parameters for the ICM and LMXB models, except for the ICM component. The ratio of the two APEC normalizations is tied to that of the *Chandra* model but not the overall normalizations to allow for the cross-calibration uncertainty of *NuSTAR* and *Chandra* and the difference in response due to the much larger PSF of *NuSTAR*. The difference in best-fit normalizations turns out to be small, with less than a 1% difference when constraining the overall hard X-ray emission from the AGN activities (this section) and about 6% when decomposing the core emission from the knots/jet (Section 4).

The best-fit spectra with all the model components are shown in Figure 2. The best-fit power-law index of the overall AGN-related emission is $\Gamma = 2.12^{+0.12}_{-0.13}$ and the associated 20–40 keV flux, which completely dominates the spectrum, is $7.7^{+1.1}_{-1.0} \times 10^{-13} \text{erg cm}^{-2} \text{s}^{-1}$. The spectrum is well characterized by a single power law with no evidence of cut-off in energy below $\sim 100 \text{keV}$ (3σ).¹¹

The 20–40 keV flux measured is an order of magnitude lower than that determined by de Jong et al. (2015) with the *Suzaku* observation taken in 2006. It is believed that the X-ray emission above 20 keV detected near the end of 2006 was due to the HST-1 flare (de Jong et al. 2015; Prieto et al. 2016). The *Chandra* observations in 2017 show that the soft emission ($\lesssim 10 \text{keV}$) from HST-1 has become fainter by a factor of ~ 40 since 2006 November. By simple scaling, the contribution from HST-1 in 20–40 keV should be a factor of a few lower than that from the core. This is indeed the case where HST-1 is a factor of six fainter than the core in 2017 measured in this band (Section 4). Therefore, for the first time, we have detected hard X-ray emission above $\sim 10 \text{keV}$ dominated by the core, which also gives the upper limit of its quiescent emission in hard X-rays.

4. DECOMPOSING THE HARD X-RAY EMISSION OF THE CORE, HST-1, AND JET

¹¹ The lower limit of the cut-off energy is determined by the fitting of a cut-off power-law model (`cutoffpl1`).

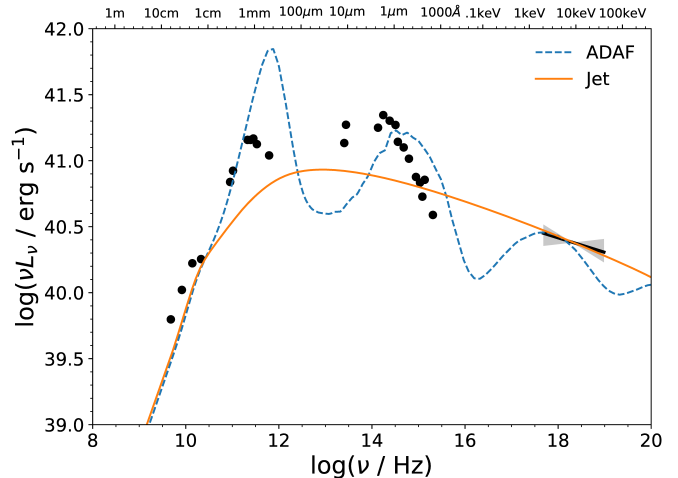


FIG. 4.— SED of the core with X-ray data taken from this work (90% confidence region in photon index shown in gray) and the rest taken from the $0''.4$ quiescent data points of Prieto et al. (2016). The ADAF and jet models were taken from Nemmen et al. (2014) and renormalized to match the X-ray data.

We can further constrain the individual components of the core, HST-1, and the rest of the knots and jet by joint fitting the corresponding *Chandra* spectra. We model each of these components as a single power law. The power-law indices of these components are tied for the *NuSTAR* and *Chandra* spectra. HST-1 and jet emission is subdominant, and therefore their normalizations are tied for the *NuSTAR* and *Chandra* spectra. The normalizations of the core component for *NuSTAR* and *Chandra* are not tied, to allow for calibration uncertainty.

The best-fit spectra with all the model components are shown in Figure 3. The best-fit power-law index of the core is $\Gamma = 2.11^{+0.15}_{-0.11}$ and the associated 20–40 keV flux measured with *NuSTAR* is $4.8^{+0.9}_{-1.0} \times 10^{-13} \text{erg cm}^{-2} \text{s}^{-1}$, which is about 60% of the overall AGN emission. The normalization measured with *Chandra* is about 10% lower and smaller than the statistical uncertainty of about 20%. Such consistency suggests that the assumed power-law models for different components are reasonable. The 20–40 keV flux of HST-1 and the jet are about 16% and 37% of the core, respectively. The best-fit parameters for the three components and the overall AGN emission are listed in Table 1.

5. DISCUSSION

We have detected hard X-ray emission from the M87 core, which can be readily compared with model predictions. We focus on a few recent models with hard X-ray predictions based on the full SED constrained within $<1''$ from the core (Prieto et al. 2016).

Figure 4 shows the SED of the M87 core, together with the ADAF-dominated and jet-dominated models of Nemmen et al. (2014). Both models were renormalized to match the X-ray data. In the past, it was difficult to distinguish these two models since both of them fit the SED well and predict similar slopes in soft X-rays below 10 keV (see, e.g., Nemmen et al. 2014). With *NuSTAR* data extending to 40 keV, it is quite clear that the X-ray slope predicted by the ADAF-dominated model is too steep, while the X-ray slope and also the global SED

are more consistent with the jet-dominated model. Note that the featureless emission of a jet probably cannot explain the entire SED, particularly the IR to UV bump seen in the data. A global fitting by varying the parameters of both the ADAF and jet components instead of simply renormalizing the models is needed to address the problem correctly.

Recently, with Faraday rotation measure observations, it has become clearer that the X-ray emission is more jet-dominated (Feng et al. 2016; Li et al. 2016). Our joint *NuSTAR* and *Chandra* observations provide additional insights into these models. For example, our best estimated SED at 40 keV ($\sim 10^{19}$ Hz) is $\nu F_\nu = 6.6^{+1.5}_{-1.3} \times 10^{-13} \text{ erg cm}^{-2} \text{ s}^{-1}$, which is consistent with the jet model predicted by Prieto et al. (2016). However, by inspecting the X-ray slope in their Figure 3, the predicted photon index is $\Gamma \lesssim 2$, which is marginally flatter than our measured index of $2.11^{+0.15}_{-0.11}$. Comparing with model predictions by Li et al. (2016), our result is marginally consistent with the jet-dominated model ($\approx 5 \times 10^{-13} \text{ erg cm}^{-2} \text{ s}^{-1}$) and slightly higher than the ADAF-dominated model ($\approx 3 \times 10^{-13} \text{ erg cm}^{-2} \text{ s}^{-1}$). The measured photon index is also slightly more consistent with the jet-dominated model (≈ 2.1) than the ADAF-dominated model (≈ 2.2). Note that the reason for not

being able to completely rule out one model in favor of another (jet-dominated versus ADAF-dominated) is related to the theoretical uncertainties and freedoms allowed in the modeling.

In order to explain γ -ray and TeV emission from M87, the SED has been modeled using the synchrotron self-Compton (SSC) model that fits the softer X-ray ($\lesssim 10$ keV) and above γ -ray emission fairly well during the quiescent state of the core (Figure 3 in de Jong et al. 2015, also, Figure 4 in Abdo et al. 2009). However, they overpredict the hard X-ray (~ 40 keV) emission measured with *NuSTAR* by a factor of about three. Their predicted power-law index (~ 1.6) near 40 keV is also significantly flatter than the measured value. *NuSTAR* is probing the transition from synchrotron dominant to (self) inverse Compton dominant emission around 10 keV and is providing the key information on these VHE processes. Currently, the uncertainties are limited by the statistics of our data. A deep *NuSTAR* observation extending detection beyond 40 keV, and simultaneous high angular resolution multi-wavelength observations, will provide further constraints on accretion models and VHE emission mechanisms.

We thank the referee for helpful comments. This work was supported by NASA *Chandra* grant GO7-18085X and NASA *NuSTAR* grant NNX17GF12P.

REFERENCES

- Abdo, A. A., Ackermann, M., Ajello, M., et al. 2009, *ApJ*, 707, 55
 Abramowski, A., Acero, F., Aharonian, F., et al. 2012, *ApJ*, 746, 151
 Aharonian, F., Akhperjanian, A. G., Bazer-Bachi, A. R., et al. 2006, *Sci*, 314, 1424
 Biretta, J. A., Sparks, W. B., & Macchetto, F. 1999, *ApJ*, 520, 621
 Cappellari, M., Emsellem, E., Krajnović, D., et al. 2011, *MNRAS*, 413, 813
 Curtis, H. D. 1918, *Publications of Lick Observatory*, 13, 31
 de Jong, S., Beckmann, V., Soldi, S., Tramacere, A., & Gros, A. 2015, *MNRAS*, 450, 4333
 Doeleman, S. S., Fish, V. L., Schenck, D. E., et al. 2012, *Science*, 338, 355
 Feng, J., Wu, Q., & Lu, R.-S. 2016, *ApJ*, 830, 6
 Gebhardt, K., & Thomas, J. 2009, *ApJ*, 700, 1690
 Harris, D. E., Cheung, C. C., Biretta, J. A., Sparks, W. B., Junor, W., Perlman, E. S., & Wilson, A. S. 2006, *ApJ*, 640, 211
 Harris, D. E., Cheung, C. C., Stawarz, L., Biretta, J. A., & Perlman, E. S. 2009, *ApJ*, 699, 305
 Junor, W., Biretta, J. A., & Livio, M. 1999, *Nature*, 401, 891
 Kalberla, P. M. W., Burton, W. B., Hartmann, D., Arnal, E. M., Bajaja, E., Morras, R., & Pöppel, W. G. L. 2005, *A&A*, 440, 775
 Kovalev, Y. Y., Lister, M. L., Homan, D. C., & Kellermann, K. I. 2007, *ApJ*, 668, L27
 Krivonos, R., Revnivtsev, M., Churazov, E., Sazonov, S., Grebenev, S., & Sunyaev, R. 2007, *A&A*, 463, 957
 Li, Y.-P., Yuan, F., & Xie, F.-G. 2016, *ApJ*, 830, 78
 Macchetto, F., Marconi, A., Axon, D. J., Capetti, A., Sparks, W., & Crane, P. 1997, *ApJ*, 489, 579
 Nemmen, R. S., Storchi-Bergmann, T., & Eracleous, M. 2014, *MNRAS*, 438, 2804
 Perlman, E. S., Sparks, W. B., Radomski, J., Packham, C., Fisher, R. S., Piña, R., & Biretta, J. A. 2001, *ApJ*, 561, L51
 Prieto, M. A., Fernández-Ontiveros, J. A., Markoff, S., Espada, D., & González-Martín, O. 2016, *MNRAS*, 457, 3801
 Revnivtsev, M. G., Sunyaev, R. A., Krivonos, R. A., Tsygankov, S. S., & Molkov, S. V. 2014, *Astronomy Letters*, 40, 22
 Russell, H. R., Fabian, A. C., McNamara, B. R., & Broderick, A. E. 2015, *MNRAS*, 451, 588
 Tonry, J. L., Dressler, A., Blakeslee, J. P., Ajhar, E. A., Fletcher, A. B., Luppino, G. A., Metzger, M. R., & Moore, C. B. 2001, *ApJ*, 546, 681
 Wik, D. R., Hornstrup, A., Molendi, S., et al. 2014a, *ApJ*, 792, 48
 Wik, D. R., Lehmer, B. D., Hornschemeier, A. E., et al. 2014b, *ApJ*, 797, 79
 Wong, K.-W., Irwin, J. A., Shcherbakov, R. V., Yukita, M., Million, E. T., & Bregman, J. N. 2014, *ApJ*, 780, 9
 Yuan, F., & Narayan, R. 2014, *ARA&A*, 52, 529